

P. Sandquist, S.E. Sharapov, M. Lisak, T. Johnson
and JET-EFDA contributors

Bi-Directional Tornado Modes on JET

"This document is intended for publication in the open literature. It is made available on the understanding that it may not be further circulated and extracts or references may not be published prior to publication of the original when applicable, or without the consent of the Publications Officer, EFDA, Culham Science Centre, Abingdon, Oxon, OX14 3DB, UK."

"Enquiries about Copyright and reproduction should be addressed to the Publications Officer, EFDA, Culham Science Centre, Abingdon, Oxon, OX14 3DB, UK."

Bi-Directional Tornado Modes on JET

P. Sandquist¹, S.E. Sharapov², M. Lisak¹, T. Johnson³
and JET-EFDA contributors*

¹*EURATOM-VR Association, and Department of Radio and Space Science, Chalmers University of Technology,
SE-412 96 Göteborg, Sweden*

²*EURATOM-UKAEA Fusion Association, Culham Science Centre, OX14 3DB, Abingdon, OXON, UK*

³*EURATOM-VR Association, Alfvén Laboratory, Royal Institute of Technology, 10044 Stockholm, Sweden*

** See annex of M.L. Watkins et al, "Overview of JET Results ",
(Proc. 21stIAEA Fusion Energy Conference, Chengdu, China (2006)).*

ABSTRACT.

In discharges on the Joint European Torus (JET) with safety factor $q(0) < 1$ and high power Ion Cyclotron Resonance Heating (ICRH), monster sawtooth crashes are preceded by sweeping frequency ‘tornado modes’ in the TAE frequency range. A suite of equilibrium and spectral MHD codes is used for explaining the observed evolution of the tornado mode frequency and for identifying temporal evolution of the safety factor inside the $q = 1$ radius just before sawtooth crashes. In some cases, the tornado modes are observed simultaneously with both positive and negative toroidal mode numbers. Hence, a free energy source other than the radial gradient of the energetic ion pressure exciting these modes is sought. The distribution function of the ICRH-accelerated ions is assessed with the SELFO code and energetic particle drive due to the velocity space anisotropy of ICRH-accelerated ions is considered analytically as the possible source for excitation of bi-directional tornado modes.

1. INTRODUCTION

The physics of highly energetic ions in tokamak plasmas is one of the most important burning plasma topics [1] and is investigated on JET. Instabilities of high-frequency waves (50-500 kHz for typical JET parameters) are often excited in JET by resonant interaction between shear Alfvén waves and super-Alfvénic energetic ions accelerated by Ion-Cyclotron Resonance Heating (ICRH) [2] or by ions produced with Neutral Beam Injection (NBI) [3]. Similar excitation of Alfvén instabilities by fusion-born alpha-particles may occur in the burning fusion plasma of ITER, since for typical ITER parameters the Alfvén speed is just below the velocity of fusionborn alpha-particles at birth. Possible interplays between the high-frequency Alfvén instabilities and low-frequency MHD modes, such as sawtooth oscillations in discharges with the central safety factor $q(0) < 1$ [4, 5] are of major interest for burning plasmas since both Alfvénic and sawtooth instabilities may become strongly coupled through the same population of energetic ions.

When a significant population of energetic ions is accelerated up to the MeV energy range by high power ICRH in sawtoothing JET discharges, the sawtooth oscillations change their character significantly and become so-called monster sawtooth oscillations [6]. In contrast to sawteeth in Ohmically heated plasmas, the monster sawtooth oscillations have very long periods (~ 1 s or longer), saturating or even decreasing the central electron temperature, $dT_e(0)/dt \leq 0$, during the pre-crash phase, and much shorter crash times ($\sim 50 \mu\text{s}$). Monster sawtooth crashes produce larger drops in electron temperature and trigger neoclassical tearing modes more often. The long period of such sawteeth is attributed to the stabilising effect of ICRH-accelerated energetic ions [7], while the short crash time is explained by the electron inertia, which introduces a very short time scale in the Ohm’s law in a singular layer surrounding the $q = 1$ magnetic flux surface [8]. However, some characteristics of the monster sawtooth behaviour, such as the saturation or decrease of electron temperature at the pre-crash phase, as well as the very occurrence of the crash while the fast ion stabilisation persists, were more difficult to explain.

It was suggested that $n = 1$ fishbone oscillations preceding the crashes of monster sawteeth may

expel fast ions from inside the $q = 1$ radius, thus triggering loss of fast ion stabilisation with subsequent crashes [7]. However, it was then found that not all crashes have pre-cursors in the form of fishbones, and a search for alternative possibilities continued. In the late-nineties, significant improvements made in the detection of Alfvénic instabilities allowed an identification of another precursor to monster sawtooth crashes – so-called 'tornado' modes [9–11] with frequencies much higher than the frequency of the $n = 1$ fishbones. Frequencies of these multiple modes are close to the frequency range of Toroidal Alfvén Eigenmodes (TAEs), but in contrast to the usual TAEs, they exhibit a significant sweep in frequency and are observed with mode numbers decreasing one-by-one during the time preceding the sawtooth crashes. Due to the sweeping frequency evolution, tornado modes were first associated with Energetic Particle Modes (EPMs). It was noted from the very beginning [9] that tornado modes cause a much more significant degradation of the fast ion confinement than TAEs. It was also suggested [10] that the very occurrence of the monster sawtooth crash may be caused by the tornado modes expelling fast ions from the central region of plasma inside the $q = 1$ radius, so that the fast ion stabilising effect decreases below a critical value and the sawtooth crash can no longer be prevented by the fast ions. In accordance with such theory, the saturation or decrease of electron temperature, $dT_e/dt \leq 0$, at the pre-crash phase, is not caused by a sudden change in electron heat conductivity. Instead, a saturation or decrease of the electron heating source causes the electron temperature to roll over as the fast ion pressure gradient exceeds the critical value for excitation of tornado modes and these modes expel fast ions from the centre of the plasma to the region outside the $q = 1$ magnetic surface.

In parallel, a theory of low-shear TAEs was developed in order to explain modes observed in TFTR DT experiments, in which the values of β exceeded the critical threshold for TAE suppression [12, 13]. However, it was only understood after observation of 'odd' tornado modes on JET that the tornado modes are not EPMs as suggested in [10], but they are low-shear TAEs inside the $q = 1$ radius [14]. The significant frequency sweep of tornado modes and the sequence of toroidal mode numbers are caused by the proximity of the modes to the magnetic axis and by $q(0)$ decreasing in time; both effects were established in ideal MHD modelling with MISHKA and NOVA-K codes [14].

The identification of tornado modes as low-shear TAEs inside the $q = 1$ radius made it possible to model these modes and to develop a dedicated experimental scenario for studying tornadoes in JET plasmas with monster sawteeth [2]. It was noted in [14] that tornado modes are localised deep in the plasma core and they rarely have more than two coupled poloidal harmonics. Under such conditions, it became clear that detection of tornado modes is a significantly more difficult task than detection of TAEs outside the $q = 1$ radius, since TAEs are closer to the magnetic pick-up coils (Mirnov coils) outside the plasma, and TAEs consist of multiple harmonics due to greater magnetic shear outside the $q = 1$ radius. The progress in detecting Alfvén Eigenmodes with core plasma diagnostics on JET such as interferometry [15–17] and reflectometry [18] made it possible to observe tornado modes even if these were localised very close to the magnetic axis and thus were not seen by Mirnov coils.

Recent JET experiments devoted to tornado modes have revealed that in many cases tornado modes with both positive and negative toroidal mode numbers are observed simultaneously. The spectroscopic analysis resembles the study previously done in [19], where the sequence of TAE excitation prior to sawtooth crashes, as well as EAE excitation following the sawtooth crashes were studied. It is our intention to study the experimentally observed bi-directional EAEs in another paper.

In cylindrical geometry, shear Alfvén waves satisfy the dispersion relation $\omega = |k_{\parallel m}(r)v_A(r)|$, where $k_{\parallel m}(r)$ is the parallel component of the wave vector as a function of minor radius r and $v_A(r) = B_0/\sqrt{4\pi\rho_0}$ is the Alfvén velocity. However, these waves suffer from strong continuum damping. In tokamaks, the toroidal geometry introduces perturbations, known as toroidal coupling terms, which lead to a coupling between neighbouring poloidal harmonics of the wave [20, 21], expressed by the coupling condition

$$k_{\parallel m}(r_m) = -k_{\parallel m-1}(r_m) \quad (1)$$

The resulting TAE gap structure supports discrete frequency TAEs at magnetic flux surfaces characterised by

$$q(r_m) = \frac{m - 1/2}{n} \quad (2)$$

where m and n are the poloidal and toroidal mode numbers, respectively, in the Fourier decomposition of the wave. Moreover, the frequency of TAEs within the TAE gap range is given by [22]

$$\omega^2_{TAE} \simeq \left(\frac{v_A(r)}{2q(r)R_0} \right)^2 \left(1 \pm \frac{5}{2} \frac{r}{R_0} \right)^2 \quad (3)$$

where R_0 is the major radius of the torus.

TAEs can be modelled with MHD codes in order to verify the experimentally observed bi-directional modes. However, whereas MHD modelling of TAEs gives a deeper understanding of plasma equilibrium properties, mode locations and mode widths, it does not consider the question of drive necessary for the excitation of the bi-directional tornado modes. The drive coming from a monotonically decreasing pressure is only positive for modes propagating in the ion diamagnetic direction, which corresponds to propagation in the same direction as inductive current (co-propagation) on JET. Mathematically, the necessary condition for a positive drive of TAEs due to hot ions is $\omega < \omega_*$ [21], where the diamagnetic frequency is given by

$$\omega_* = \frac{nv}{w_c R_0} \frac{\partial f_0 / \partial J_\psi}{\partial f_0 / \partial v} \quad (4)$$

Here, f_0 is the unperturbed hot ion velocity distribution function, J_ψ is the toroidal canonical momentum, $w_c = eB_0/cM$ is the cyclotron frequency, where M is the particle mass, and v is the

particle velocity. In order to explain counter-propagating tornado modes with $n < 0$, the drive coming from fast ion anisotropy in the velocity space [23] has to be considered. Analytic theory for the drive was previously carried out in [24], where the stabilising effects due to the mode structure was considered for excitation by both passing and trapped hot ions in a small banana width limit.

The paper is organised as follows. In Section II, experimental data for tornado mode Pulse No: 66203 of the tornado mode session on JET is presented. The existence of the observed bi-directional tornado modes are then verified, by a suite of MHD codes, in Section III. Theory for bi-directional tornado mode drive, arising from velocity anisotropy in the ICRH-accelerated fast ion distribution function, is presented and applied to experimental data in Section IV. Finally, we summarise and discuss the results obtained in Section V.

2. EXPERIMENTAL OBSERVATIONS ON JET

Figure 1 shows electron temperature, line-average electron density, and power waveforms in JET discharge (Pulse No: 66203) with magnetic field 2.7T and plasma current 2MA, where bi-directional tornado modes were observed.

High power ICRH with a frequency corresponding to the hydrogen cyclotron frequency at the magnetic axis was used for accelerating hydrogen minority ($n_{\text{H}}/n_{\text{e}} \approx 2.5\%$) ions, so that ICRH generated an energetic tail of hydrogen ions and, via the second harmonic resonance, some deuterium tail. Low-power blips of NBI were used for measuring the ion temperature and the safety factor profile. An inductive current flat top of 2 MA was obtained one second before the start of ICRH, and short-period sawteeth in the Ohmic phase of the discharge appeared before ICRH power was applied. The transition from Ohmic sawteeth to monster sawteeth is shown in Figure 2.

In this discharge, eight monster sawteeth were observed as can be seen from Te measurements in Figure 1, and all of them were preceded by bi-directional tornado modes. Figures 3 (a)–(c) show the examples of bi-directional tornado modes preceding the first monster sawtooth crash at $\sim 11.3\text{s}$.

Figure 3 (a) shows toroidal mode numbers of the poloidal magnetic field perturbations derived from the phase shifts between signals measured with toroidally separated Mirnov coils located just outside the plasma. The toroidal mode numbers of the co-current propagating modes with positive n are seen to decrease in time one-by-one from $n = 9$ to $n = 2$ as the sawtooth crash approaches. The counter-propagating modes with negative toroidal mode numbers display a less regular sequence of appearance occurring simultaneously with $n = -6, -5$, and, somewhat later, with $n = -4$ and $n = -2$.

Figures 3 (b), (c) show spectrograms of electron density perturbations detected in the same frequency range with the O-mode interferometry [15]. Figures 3 (a) and 3 (b) show that tornado modes with both positive and negative mode numbers are detected with Mirnov coils and O-mode interferometry. However, the O-mode interferometry also shows a set of sweeping frequency Alfvén cascades in the range 50–150kHz, which were hardly visible by using the Mirnov coils.

In order to clarify the co-existence of Alfvén cascades and tornado modes, another example of tornado modes preceding sawtooth crash is shown in Figure 4. Figure 4 shows, somewhat clearer

than in Figure 3 (c), an image of both Alfvén cascades and tornado modes detected with the O-mode interferometry. Although there is a frequency gap 200–220kHz separating Alfvén cascades and tornado modes, this figure suggests that tornado modes may be related to Alfvén cascades in this case. It is important to note that Alfvén cascades in the low-shear region inside the $q = 1$ radius, in contrast to the advanced tokamak scenarios with $q > 1$, may not be necessarily associated with a reversed magnetic shear. At least two other effects may play a role in forming the Alfvén cascade eigenmodes very close to the magnetic axis, namely (i) magnetic axis itself may form a potential barrier in ideal MHD providing a sufficiently flat (but still monotonic) q -profile [25], and (ii) the FLR effects of thermal ions may form Rosenbluth-Rutherford modes in the vicinity of the magnetic axis [26].

Taking into account that the experimental data shows only one set of Alfvén cascade eigenmodes in Figures 3 (c) and 4, it is unlikely that these modes have negative toroidal mode numbers, which would be shifted in frequency due to the Doppler shift. Since the problem of explaining the bi-directional tornado modes seems to be independent of the relation between tornado modes and Alfvén cascades, we focus here on the bi-directional modes in the TAE frequency range only in what follows, while the very interesting question about the coupling of tornado modes and Alfvén cascades will be considered elsewhere.

It is of special interest to consider bi-directional tornado modes during NBI. The unbalanced beam injection on JET spins up the plasma toroidally and this toroidal rotation causes Doppler shift in frequencies of modes with different toroidal mode numbers. In this way, frequencies of positive and negative mode numbers are well separated and it makes the analysis of the data less ambiguous. Figure 5 shows bi-directional tornado modes during NBI as these are observed with Mirnov coils. Figure 6 shows high-frequency density perturbations detected with the O-mode interferometry at the same time. No Alfvén cascades are detected by interferometry in this case.

Figure 5 shows the results of a toroidal mode number analysis of JET Pulse No: 66203 just before a giant sawtooth crash at $t = 20.2$ s. The excitation of tornadoes with negative mode numbers, $n < 0$, is delayed in comparison to the excitation of positive mode number ($n > 0$) tornadoes. Moreover, some of the counter-propagating modes are upward-chirping whereas copropagating modes are downward-chirping. From the observation of negative mode number tornadoes, our first idea was that we are most likely to have a hollow fast ion pressure profile in these discharges due to low-field side ICRH. However, modelling of the ICRH-accelerated distribution function with the self-consistent code SELFO [27] shows that this is not the case at the time of excitation of tornado modes. Possible explanations of the observation of negative toroidal mode number tornadoes are discussed further in Section IV.

We note that at about twice the TAE range of frequencies, bi-directional EAEs are found to be excited after the sawtooth crash, when the safety factor profile has been lifted due to the effect of the reconnection event. Since Alfvén cascades are also observed as Figs.3 (c) and 4 show, we are in a position to test whether a reversed shear safety factor profile better models the observed temporal

evolution of tornado modes in Fig. 5. In Section III, this idea is further investigated.

3. MODELLING WITH MHD CODES

The experimental observations of bi-directional tornado modes on JET are investigated further below with a suite of MHD codes; HELENA [28], CSCAS [29] and MISHKA [30, 31]. The aim of the MHD modelling is to identify the radial location of the tornado modes, to verify the toroidal mode numbers suggested by the mode number analysis, and to reproduce the temporal evolution of the mode frequencies. where θ and ζ are the poloidal and toroidal coordinates, and B_θ and B_ζ are the toroidal and poloidal magnetic field components. Since $B_\theta/B_\zeta \sim \mathcal{O}(\epsilon)$, equation (5) states that $q \sim \mathcal{O}(1)$. In order to study the possibility of a reversed magnetic shear scenario, a reversed shear equilibrium just outside the error bars of MSE diagnostics as well as a reversed shear equilibrium from a similar type of discharge, but with larger negative magnetic shear, have been generated. The safety factor profiles of the three basic equilibria used for tornado mode modelling are illustrated in Fig.7.

A. EQUILIBRIUM RECONSTRUCTION

The MHD code HELENA [28] is first used to construct an equilibrium in straight field line coordinates from a Motional Stark Effect (MSE) measured safety factor profile. The safety factor is defined through

$$q(r) = \frac{B \cdot \nabla \zeta}{B \cdot \nabla \theta} \simeq \frac{r B_\zeta}{R_0 B_\theta} \quad (5)$$

B. ALFVÉN EIGENMODE MODELLING

The Alfvén Continuum Gap (ACG) structure, which is generated with the CSCAS code [29] and is modified as the value of the safety factor changes, provides a graphical way to determine the radial positions and normalised frequency range of possible TAEs. In particular, since the safety factor profile is included in the ACG structure diagram, it is instructive to consider the CSCAS output in order to judge whether TAEs are to be located outside the $q = 1$ surface, or inside the $q = 1$ surface, in which case they are called tornado modes.

Starting from the reconstructed MSE equilibrium, a sweep in the safety factor value on the magnetic axis is performed with the HELENA code. For each value of $q(r = 0) = q_0$, the MHD spectral code MISHKA [30, 31] is used in order to scan the Alfvén continuum gap structure, observed in CSCAS for tornado modes. An initial guess of the normalised eigenmode frequency,

$$\bar{\omega} = \frac{w R_0}{v_A} \quad (6)$$

is then made. Note that the centre of the TAE gap corresponds to normalised frequency $\bar{\omega} = 1/2$ (see Eq.(3)). A complete scan of the TAE gap in this way finds all the supported modes by the specific $q_0 = \text{const}$ equilibrium.

The supported modes consist of two dominant poloidal harmonics, for which the poloidal mode number m is consistent with the coupling condition, Eq. (1). Representative tornado mode structures for $n = +4, +5$ and $+6$ are illustrated, together with the ACG structure from CSCAS, in Figs. 8–10.

As the modelled TAEs inside $q = 1$ are shifted radially outwards, due to a decrease in q_0 , they start to couple to edge-localised modes. In order to minimise this coupling, it is appropriate to consider a larger number of grid points and to introduce a perfectly conducting wall in MISHKA [32].

3.3 MODELLING RESULTS

In order to describe the results of bi-directional tornado mode modelling, we assume (i) a linear decrease of q in time, and (ii) the radial gradient of $q(r)$ from MSE measurements is constant at all times. This facilitates a linear mapping of the modelled decrease in q_0 to the temporal evolution of the normalised tornado mode frequencies. Furthermore, we map the normalised frequency ω by taking the values $\omega_A(r = 0) = 7.9$ Mm/s and $R_0 = 3.0$ m, and including the experimentally observed Doppler shifts. The validity of considering only constant values for the Alfvén velocity is confirmed by LIDAR Thompson scattering measurements of electron density. The plasma rotation frequency is measured by charge exchange, and the measured frequency in the laboratory frame is given by

$$f_{lab} = f_{TAE} + n f_{rot} \quad (7)$$

where $\omega_{TAE} = 2\pi f_{TAE}$ is the TAE frequency in the rest frame, Eq. (3), and $f_{rot}(r = 0.4) = 2.3$ kHz at $t = 20$ s in our discharge, JET Pulse No: 66203. The results of the MSE equilibrium modelling are presented in Fig. 11, from which a good agreement with the experimental data in Fig. 5 is confirmed.

From Figs. 3 (c) and 4, we learn that evidence for a reversed shear scenario exists. Therefore, we proceed with two reversed shear safety factor equilibria; the one constructed from the MSE measured equilibrium (just outside MSE error bars) and the one that uses an invented, strongly reversed safety factor from JET Pulse No: 54956. These two additional safety factor profiles are depicted in Fig. 7. The proposed idea consists of identifying (i) $\hat{s} > 0$ positive tornadoes, where $\hat{s} = (r/q)dq/dr$ is the magnetic shear of the safety factor profile, (ii) $\hat{s} > 0$ negative tornadoes associated with the same magnetic surface, and (iii) $\hat{s} < 0$ negative tornadoes, which appear late before the sawtooth crash and are associated with a magnetic surface with a value of q one step lower than the previous one, see Eq. (2). The third group of tornado modes would then complete the “corridor” of tornado modes located at two different radii and expel resonant hot ions, potentially giving rise to the sawtooth crash.

Apart from being able to handle three groups of tornado modes, the reversed shear scenario would be able to give rise to a group of multiple Low-Shear TAEs (LSTAEs). For a low enough shear, the number of LSTAEs is given by the scaling formula [33]

$$N_{LSTAE} \sim \epsilon/\hat{s} \quad (8)$$

The minimum of the reversed shear safety factor profile, q_{\min} , for this profile is then artificially moved radially inwards in order to obtain two to three LSTAEs. We modify the polynomial coefficients of the expression for the amplitude of the two flux functions in the Shafranov equation, from which the HELENA equilibrium is obtained. The two to three LSTAEs found in this way have the correct frequency chirping and frequency spacing in order to explain the lower group of $n < 0$ tornadoes.

However, the difference in frequencies between the upper and lower groups of counterpropagating tornado modes is found to be too high – a factor of $q(r_6)/q(r_5) \big|_{n=6} = 0.917/0.75$ due to different resonant flux surfaces (see Eq. (2)). This would actually make the upper group of counter-propagating modes higher in frequency than the co-propagating modes, in contradiction to what is experimentally observed and illustrated in Fig.5. The idea of having a reversed shear equilibrium is therefore abandoned.

Returning to the modelling of the MSE measured safety factor profile equilibrium, we explain the change in spectral behaviour of the tornado modes, both positive and negative, around $t = 20$ s, by a formation of global TAEs. A similar transition, from local to global Alfvén eigenmodes, was reported in Ref. [32]. The reason for the transition to global structure comes from an increase of the shear \hat{s} as the mode moves radially outwards, locked at a position determined by Eq. (2). After the modes have transformed into a global structure, their spectroscopic use for determining the safety factor, $q(r)$, is lost [32].

We note that our modelling results are in agreement with the co-propagating tornado modes and the lower counter-propagating tornado modes, but an explanation of the multiplicity of the two groups of counter-propagating modes for $t \approx 20.1$ s, i.e. just before the sawtooth crash, also seen in Fig.5, has to be sought. These additional counter-propagating tornado modes are not seen in any other of the six sawtooth crashes in JET Pulse No: 66203, so perhaps it is not statistically justified to give an account of these tornado modes.

IV. TAE GROWTH RATE THEORY

Several theoretical models have predicted the presence of TAE instability due to the resonant interaction with hot ions, cf. [21, 34], where it has been shown that the TAEs can be strongly excited if the mode frequency ω is lower than the diamagnetic frequency of the fast ions, ω_* . In [24], a generalised expression for the linear growth rate of the TAEs, which takes into account the large particle orbit width effects and the effect of mode localisation as well as the excitation by both passing and trapped hot ions, is derived. An application of this theory to a strongly anisotropic slowing-down velocity distribution generated by NBI and of fusion produced alpha particles has shown that stabilisation of the TAE instability due to large particle orbit width is much more pronounced in the case of an isotropic alpha particle velocity distribution. Here, we analyse the general expression for the TAE instability growth rate with respect to the role of the anisotropy in the hot particle velocity distribution.

According to [24, 35], the destabilisation of TAEs is sensitive to the ratio between the radial excursion of the hot particle orbits from the flux surfaces, Δ_b , and the TAE localisation scale length, Δ_m . In the limit of low magnetic shear and large mode numbers, the inner and outer mode structure of the TAE can be described by [22]

$$\Phi_m^{(i)} = C_m \left[\frac{1}{\alpha_m} \arctan \left(\frac{r - r_m}{\Delta_m^{(i)}} \right) + \frac{1}{2} \ln \left| \left(\frac{r - r_m}{\Delta_m^{(i)}} \right)^2 + 1 \right| \right] + \text{const} , \quad (9)$$

$$\Phi_m^{(o)} = -C_m K_0 \left(\left| \frac{r - r_m}{\Delta_m^{(o)}} \right| \right) , \quad (10)$$

where $K_0(x)$ is the zeroth order MacDonal function, $\alpha_m = 4/(\pi\hat{s})$, \hat{s} is the magnetic shear, r_m is the mode localisation radius, R_0 is the major radius at the magnetic axis, $\Delta_m^{(i)} = (\pi/8)dr_m^2/R_0$ with $d = 2.5-5$ and (o) $\Delta_m^{(o)} = r_m/m$ are the inner and outer widths of the mode, respectively, and C_m is a constant determined by the boundary conditions at the gap surface. Note that, in spite of the fact that $\Delta_m^{(i)}/\Delta_m^{(o)} = r_m/R_0 \ll 1$, most of the mode energy is concentrated in the inner region of the mode. For well-passing particles it can be estimated that $\Delta_b^p \approx qv/\omega_c$, where ω_c is the particle cyclotron frequency, which for ω_*/ω gives $\Delta_b^p/\Delta_m^{(o)} > 1$. For trapped particles, the width of the banana orbits is $(\Delta_b^t)_{max} \approx 2\sqrt{2}q_m/\kappa_{max}v/(\omega_c\epsilon_m^{1/2})$, where $\epsilon_m = r_m/R_0$, implying that $\Delta_b^p/\Delta_m^{(i)} > 1$ can be satisfied. Furthermore, the excursion of particle orbits can be comparable to or larger than the orbit of the excited TAE mode, i.e. $\Delta_b \geq \Delta_m^{(o)} \geq r_m/m$ for passing particles and $qv_A/\omega_c \geq \sqrt{\epsilon_m}r_m/m$ for trapped particles, where $v_A = B_0/\sqrt{4\pi\rho_0}$ is the Alfvén velocity.

The general expression for the TAE instability growth rate is given by [24]

$$\gamma = \frac{4\pi^3 e_i^2}{c^2 w_r M^2} \frac{\sum_{s,m,\sigma} \int dJ_\varphi \int E dE \int (1/\omega_b) d\lambda d\delta (\omega_r + m\langle\dot{\theta}\rangle - n\langle\dot{\phi}\rangle - s\omega_b) |G_m|^2 \hat{\Pi} f_0}{\sum_m \int dr r (|\Phi'_m|^2 + (m^2/r^2) |\tilde{\Phi}'_m|^2) v_A^{-2}} \quad (11)$$

where

$$G_m = \int_0^{\tau_b} \frac{dt}{\tau_b} v_D \left[\tilde{\Phi}'_m \sin \theta - \frac{im}{r} \tilde{\Phi}_m \left(\cos \theta - i \frac{v_\perp}{v_D} \frac{d}{d\xi} \right) \right] J_0(\xi) e^{-iS_0(0,r)} \quad (12)$$

and

$$\hat{\Pi} = \omega_r \frac{\delta}{\delta E} - \frac{\delta}{M\omega_c R_0} \frac{\delta}{\delta J_\varphi} . \quad (13)$$

Here, $\langle \cdot \rangle \int (1/\tau_b) \cdot dt$ denotes bounce averaging, ω_r is the real part of the mode frequency, $\omega_b = 2\pi/\tau_b$ is the bounce frequency, s is the bounce harmonic number, e_i and M are the ion charge and the ion mass, respectively, f_0 is the unperturbed part of the hot ion velocity distribution function, $E = Mv^2/2$ is the particle energy, $\lambda = \mu B_0/E$ is the pitch-angle variable, with $\mu = Mv_\perp^2/2B_0$ being the magnetic moment, and $J_\varphi = \Psi - hv_\parallel/\omega_c$ is the toroidal canonical angular momentum, where the poloidal flux

function is defined as $\Psi = \Psi_p/R_0 B_0 = \int R B_\theta dr/R_0 B_0$, $h = 1 + (r/R_0) \cos \theta = 1 + \epsilon \cos \theta$ and $v_{\parallel} = \mathbf{v} \cdot \mathbf{B}_0/B_0$. Furthermore, $v_D = (v_{\parallel}^2 + v_{\perp}^2/2)/R_0 \omega_c$ is the magnetic drift velocity, $\xi = k_\theta v_{\perp}/\omega_c$ is the Larmor radius parameter, $J_0(\xi)$ is the Bessel function of the first kind of zeroth order, and

$$S_0(0, t) = \int_0^t dt' (\omega_r + m\dot{\theta} - n\dot{\varphi}). \quad (14)$$

The wave field perturbation, $\tilde{\Phi}$, is described by a Fourier decomposition in poloidal harmonics according to

$$\tilde{\Phi} = \sum_m \tilde{\Phi}_m(r) e^{-im\theta + in\varphi - i\omega t}, \quad (15)$$

where θ and φ are the poloidal and toroidal angles, respectively, and n is the toroidal number. The resonance condition, expressed by the delta function in Eq. (11), is discussed below. The summation over the sign of the particle parallel velocity is included in order to incorporate trapped particles, for which $dt \sim \sigma d\theta$ and the trapped particle orbit is divided into two parts: $\sigma = +1$ for $t \in [0, \tau_b/2]$ and $\sigma = -1$ for $t \in [\tau_b/2, \tau_b]$.

In order to analyse the role of anisotropy in the hot ion velocity distribution on the instability growth rate, we follow Ref. [23] and write the operator $\hat{\Pi}$ in Eq. (13) as

$$\hat{\Pi} = \omega_r \frac{\delta}{\delta E} - \omega_r \frac{\lambda}{E} \frac{\delta}{\delta \lambda} - \frac{n}{M\omega_c R_0} \frac{\delta}{\delta J_\varphi}. \quad (16)$$

Thus the sign of the growth rate as defined by Eq. (11) is determined by the sign of the expression

$$\frac{\hat{\Pi}f_0}{\omega_r} = \left(1 - \frac{\omega_*}{\omega_r}\right) \frac{\delta f_0}{\delta E} - \frac{\lambda}{E} \frac{\delta f_0}{\delta \lambda}. \quad (17)$$

where the diamagnetic drift frequency is given by

$$\omega_* = \frac{n}{M\omega_c E_0} \frac{\delta f_0 / \delta J_\varphi}{\delta f_0 / \delta E}. \quad (18)$$

In the absence of particle anisotropy, i.e. when $\delta f_0 / \delta \lambda = 0$, and for a Maxwellian particle velocity distribution, i.e. when $\delta f_0 / \delta E < 0$, Eq. (17) implies a positive growth rate only for co-propagating modes, $n > 0$, such that the diamagnetic drift frequency satisfies $\omega_* > \omega_r$. However, anisotropy may facilitate excitation of co-propagating modes whenever $\omega_* < \omega_r$ as well as excitation of counter-propagating modes having $n < 0$. The conditions for this to occur are

$$\delta f_0 / \delta \lambda < 0, \quad (19)$$

$$|\delta f_0 / \delta \lambda| > \frac{E}{\lambda} \left| \frac{\delta f_0}{\delta E} \left(1 - \frac{\omega_*}{\omega_r}\right) \right|, \quad (20)$$

where it is still assumed that $\delta f_0/\delta E < 0$.

A TAE DRIVE DUE TO PASSING PARTICLES

In order to perform the integration along the particle orbits when calculating the growth rate explicitly we use the equations for particle drift motion

$$\dot{r} = -v_D \sin\theta, \quad (21)$$

$$\dot{\theta} = \frac{v_{\parallel}}{qR_0} - \frac{v_D}{r} \cos\theta, \quad (22)$$

$$\dot{\varphi} = \frac{v_{\parallel}}{qR_0}, \quad (23)$$

The resonance condition is determined by the delta function in Eq. (11) together with Eqs. (21)–(23). For well-passing particles it becomes

$$\omega_r - k_{\parallel m} v_{\parallel} - s\omega_b^p = 0, \quad (24)$$

where $k_{\parallel m} = (nq - m)/qR_0$, $\omega_b^p \simeq |v_{\parallel}|/qR_0$ is the bounce frequency and the superscript 'p' denotes passing particle quantities. By taking $s = \pm 1$, one finds that this resonance condition supports symmetric excitation resonances, $|v_{\parallel}| = (v_A/3, v_A)$, and passing particles can thus support counter-propagating modes.

(i) Local theory: $\Delta_b^p \ll \Delta_p^{(i)}$

For well-passing particles we find from Eqs. (21)–(23) $\Delta_b^p = v_D/\omega_c$. In the limit $\Delta_b^p \ll \Delta_m^{(i)}$, the function G_m is mainly determined by the inner mode structure. Using the fact that $|\tilde{\Phi}_m^{(i)'}(r_0)/\tilde{\Phi}^{(i)}(r_0)| \sim 1/\Delta_m^{(i)} \gg 1/\Delta_m^{(o)} \sim (r_0/m)^{-1}$, one obtains.

$$|G_m|^2 \simeq \frac{v_D^2}{4} |\tilde{\Phi}_m^{(i)'}|^2 J_0^2\left(\frac{mv_{\perp}}{r_m \omega_c}\right) (\delta_{s,1} + \delta_{s,-1}) \quad (25)$$

Substituting (25) into (11) we obtain the following expression for the growth rate

$$\begin{aligned} \frac{\gamma}{\omega_r} \frac{4\pi^3 q^2 M^2}{B_0} \sum_{v_r = v_A, v_A/3}^{v_r \sqrt{2} \epsilon} \int_0^{v_{\perp} \sqrt{2} \epsilon} v_{\perp} dv_{\perp} J_0^2\left(\frac{mv_{\perp}}{r_m \omega_c}\right) v_r \\ \times \left(v_r + \frac{v_{\perp}^2}{2}\right)^2 \left(\left(1 - \frac{\omega_*}{\omega_r}\right) \frac{\delta f_0}{\delta E} \frac{\lambda}{E} \frac{\delta f_0}{\delta \lambda} \right), \end{aligned} \quad (26)$$

where $v_{\parallel} = v_r$, $J_{\varphi} = \Psi_m$ and $\omega_r = v_A/2qR_0$. The summation over v_r in the above expression corresponds

to the possible resonances $|v_{\parallel}| = v_A$ and $|v_{\parallel}| = v_A/3$, and all quantities are calculated at $r = r_m$.

(ii) Nonlocal theory: $\Delta_m^{(i)} \ll \Delta_b^p \ll \Delta_m^{(0)}$

In this case the function G_m is still determined by the radial derivative of the inner mode structure, i.e.

$$G_m = (-1)^s \frac{v_D}{2\pi} \int_0^{2\pi} d\theta \tilde{\Phi}_m^{(i)'}(r_0 + \Delta_b^p \cos\theta) \sin\theta e^{-is\theta}, \quad (27)$$

which to the lowest order in ϵ_m leads to

$$\int_{J_{\varphi 1}}^{J_{\varphi 2}} dJ_{\varphi} |G_m|^2 \left(\frac{\omega_*}{\omega_r} - 1 \right) \frac{\delta f_0}{\delta E} - \frac{\lambda}{E} \frac{\delta f_0}{\delta \lambda} \approx \frac{C_m^2}{\Delta_m^{(i)}} \times \left[\frac{2v_D \epsilon_m^2}{\pi^2 q} I(D^p) \left(\left(\frac{\omega_*}{\omega_r} - 1 \right) \frac{\delta f_0}{\delta J_{\varphi}} - \frac{\lambda}{E} \frac{\delta f_0}{\delta \lambda} \right) \right]_{J_{\varphi} = \Psi_m}, \quad (28)$$

where $J_{\varphi 1,2} = \Psi_m - (v/\omega_c)[1 - \lambda = (2 - \lambda)\epsilon_m]^{1/2}$, $\Psi_m \sim r_m/2qR_0$, and we have used Eq. (9) to obtain

$$\Phi_m^{(i)'} = C_m \frac{(r - r_m) + \Delta_m/\alpha_m}{(r - r_m)^2 (r - \Delta_m^{(i)})^2} \quad (29)$$

Furthermore

$$I(D^p) = \int_{-D^p}^{D^p} dy \left| \int_0^{\pi} d\theta \frac{(y + D^p \cos\theta) + 1/\alpha_m}{(y + D^p \cos\theta)^2 + 1} \sin^2\theta \right|^2 \quad (30)$$

and $D^p = \Delta_b^p/\Delta_m^{(i)}$ with $\Delta_m^p \ll |r_m|$. substituting Eq. 28 into Eq. (11) together with

$$\int_{r_m - \Delta_b^p}^{r_m + \Delta_b^p} dr r \left| \Phi_m^{(i)'} \right|^2 C_m^2 \approx \frac{\pi r}{2\Delta_m^{(i)}} \quad (31)$$

and taking into account the fact that $I(D^p) \sim 2\pi^2/3D^p$ for $D^p \gg 1$ we find

$$\frac{\gamma}{\omega_r} \frac{64q^2 M^2}{3B_0^2} \sum_{v_r = v_A, v_A/3}^{v_r/\sqrt{2}\epsilon} \int_0^{v_r/\sqrt{2}\epsilon} v_{\perp} dv_{\perp} I(D^p) J_0^2 \left(\frac{mv_{\perp}}{r_m \omega_c} \right) v_r \times \left(v_r + \frac{v_{\perp}^2}{2} \right)^2 \left(\left(1 - \frac{\omega_*}{\omega_r} \right) \frac{\delta f_0}{\delta E} - \frac{\lambda}{E} \frac{\delta f_0}{\delta \lambda} \right). \quad (32)$$

(iii) Nonlocal theory: $\Delta_m^{(o)} \leq \Delta_b^p < r_m$

As long as the particle orbit excursion from the magnetic surface Δ_b^p exceeds the outer mode width $\Delta_m^{(o)}$, the function G_m is mainly determined by the outer mode structure. Using the resonance condition (24) and changing the variables according to $r = r_0 + \Delta_b^p \cos \theta$ and $\theta = \omega_b^p t$ we obtain

$$G_m = -i \frac{s\omega_b}{2\pi} \int_0^{2\pi} d\theta \tilde{\Phi}_m^{(o)'}(r_0 + \Delta_b^p \cos \theta) J_0^2 \left(\frac{mv_\perp}{r_m \omega_c} \right) e^{-is\theta} e^{iW^p \sin \theta} \quad (33)$$

with $W^p = \Delta_b^p / \Delta_m^{(o)}$. Since the mode energy is still mostly determined by the inner mode structure, we substitute (31) and (33) into (11) and obtain

$$\begin{aligned} \frac{\gamma}{\omega_r} \frac{32q^2 M^2}{B_0^2} \sum_{v_r = v_A, v_A/3}^{v_r/\sqrt{2}\epsilon} \int_0^{v_\perp/\sqrt{2}\epsilon} v_\perp dv_\perp \frac{\Delta_m^{(i)}}{\Delta_b^p} J_0^2 \left(\frac{mv_\perp}{r_m \omega_c} \right) v_r \\ \times \left(v_r^2 + \frac{v_\perp^2}{2} \right)^2 \frac{H(W^p)}{W^p} \left(\left(1 - \frac{\omega_*}{\omega_r} \right) \frac{\delta f_0}{\delta E} - \frac{\lambda}{E} \frac{\delta f_0}{\delta \lambda} \right), \end{aligned} \quad (34)$$

where

$$H(W^p) = \int_{-W^p}^{W^p} dy \left| \int_0^\pi d\theta K_0(|y + W^p \cos \theta|) \cos(-\theta + W^p \sin \theta) \right|^2 \quad (35)$$

B. TAE DRIVE DUE TO TRAPPED PARTICLES

We consider here well-trapped particles with the trapping parameter $\kappa^2 = (1 - \lambda + \lambda\epsilon)/(2\epsilon\lambda) \ll 1$ and assume narrow banana orbits, i.e. $|qv_{\parallel}/(\epsilon r \omega_c)| \ll 1$, the validity of which was confirmed with the use of the CASTOR-K code [36] for tornado modes with $n > 4$. With these assumptions and making use of the equations of particle drift motion (21)–(23) we find that

$$S_0(0, t) \approx qR_0 k_{\parallel} (\theta - \theta_1) + (\omega - \omega_D^t) t \quad (36)$$

with $\theta_1 = -2 \arcsin \kappa$ and the relation between time and the poloidal angle defined by $\omega_b^t t = \sigma [\pi/2 + \arcsin(1/\kappa \sin(\theta/2))]$. Here $\omega_b^t \approx \sqrt{(\epsilon/2)}(v/qR_0)$ is the bounce frequency and the precessional drift frequency is given by $\omega_D^t \approx nqv^2/2rR_0\omega_c$. The resonance condition becomes

$$\omega_r - \omega_D^t - s\omega_b^t = 0 \quad (37)$$

which determines the resonant velocities as

$$v_r = v_r^- = -s \frac{r\omega_c \sqrt{\epsilon/2}}{nq^2} - \sqrt{s^2 \frac{r^2 \omega_c^2 \epsilon}{2n^2 q^4} + \frac{v_A r \omega_c}{nq^2}}. \quad (38)$$

The above expression implies that for co-propagation, $n > 0$, there is only one resonant velocity v_r

$= v_r^+$ for all values of s . However, for counter-propagation, $n < 0$, both resonant velocities are possible if and only if $s > (q/r)(2|n|v_A R_0/\omega_c)^{1/2}$. For typical parameters of JET plasmas and for tornado modes with $n = [-4, -5, -6]$, this condition requires bounce harmonics satisfying $s > 4$.

(i) Local theory: $\Delta_b^t \ll \Delta_m^{(i)}$

Similarly to the case of passing particles we find that the function G_m is mainly determined by the radial derivative of the inner mode structure at $r = r_m$. Then using Eq. (36) and the equations for particle drift motion together with the resonance condition (37) for $s = 1$, we obtain

$$|G_m|^2 = \frac{v^4}{4\omega_c^2 R_0} k^2 |\Phi_m^{(i)'}| J_0^2(\xi). \quad (39)$$

Now substituting (39) into (11) and transforming the integration variable according to $d\lambda \simeq -2\epsilon d\kappa^2$, we arrive at the following expression for the growth rate

$$\frac{\gamma}{\omega_r} = \frac{4\pi^3 \sqrt{2\epsilon} q M^2}{B_0^2 R_0} J_0^2(\xi) \frac{v_A v_r^6}{D_1} \int_0^{\kappa_{max}^2} \kappa^2 d\kappa^2(\xi) \left(\left(1 - \frac{\omega_*}{\omega_r} \right) \frac{\delta f_0}{\delta E} - \frac{\lambda}{E} \frac{\delta f_0}{\delta \lambda} \right), \quad (40)$$

where v_r is given by Eq. (38) and

$$D_1 = \frac{nq v_r}{r R_0 \omega_c} + \frac{s}{q R_0} \sqrt{\frac{\epsilon}{2}}. \quad (41)$$

The above expressions take into account the effect of resonant interaction with the bounce motion and the toroidal precession motion of fast ions. The influence of the precessional drift frequency on the resonance condition can be neglected if $v_A/(\omega_c r_m) \ll \epsilon_m/(nq^2)$.

(ii) Nonlocal theory: $\Delta_m \ll \Delta_b \ll \Delta_m^{(o)}$
(i) t (o)

The function G_m is approximated as in the case of passing particles, i.e.

$$G_m = \int_0^{\tau_b^t} \frac{dt}{\tau_b^t} \Phi_m^{(i)'}(r) v_D \sin \theta e^{-iS^p(0,t)}, \quad (42)$$

which for $s = 1$ gives

$$\begin{aligned} & \int_{J_{\varphi 1}}^{J_{\varphi 2}} dJ_{\varphi} |G_m|^2 \left[\left(\frac{\omega_r}{\omega_*} - 1 \right) \frac{\delta f_0}{\delta J_{\varphi}} - \frac{\lambda}{E} \frac{\delta f_0}{\delta \lambda} \right] \simeq \frac{C_m^2}{\Delta_m^{(i)}} \frac{2J_0(\xi) v_D^2 \kappa^2 \epsilon_m}{\pi^2 q} \\ & \times \int_{-D_t}^{D_t} dy \left[\left(\frac{\omega_r}{\omega_*} - 1 \right) \frac{\delta f_0}{\delta J_{\varphi}} - \frac{\lambda}{E} \frac{\delta f_0}{\delta \lambda} \right] \left| \int_{-\pi/2}^{\pi/2} d\alpha \left[\frac{(y + D_t \cos \theta) + 1/\alpha_m}{(y + D_t \cos \alpha)^2 + 1} \right. \right. \\ & \left. \left. \times e^{-i(\alpha+\pi/2)} + \frac{(y + D_t \cos \theta) + 1/\alpha_m}{(y + D_t \cos \alpha)^2 + 1} e^{-i(\alpha+\pi/2)} \right] \sin \alpha e^{ik \sin \alpha} \right|^2, \end{aligned} \quad (43)$$

where $\Delta_b^t = 2(2/\epsilon m)^{1/2} q \kappa v / \omega_c$ is the banana width at a given value of κ and $D_t = \Delta_b^t / 2 \Delta_m^{(i)}$. Substituting (43) into (11) we obtain the following “nonlocal” expression for the TAE growth rate due to trapped particles

$$\begin{aligned} \frac{\gamma}{\omega_r} &= \frac{4\sqrt{2\epsilon} q M^2 v_A v_r^6}{B_0^2 R_0 D_1} J_0^2 \left(\frac{m v_r}{r_m, \omega_c} \right) \int_0^{\kappa_{max}^2} \kappa^2 d\kappa^2 \\ &\times \int_{-D_t}^{D_t} dy \left| \int_{-\pi/2}^{\pi/2} d\alpha \left[\frac{(y + D_t \cos \alpha) + 1/\alpha_m}{(y + D_t \cos \alpha)^2 + 1} e^{-i(\alpha+\pi/2)} \right. \right. \\ &+ \left. \left. \frac{(y - D_t \cos \alpha) + 1/\alpha_m}{(y - D_t \cos \alpha)^2 + 1} e^{i(\alpha+\pi/2)} \right] \sin \alpha e^{i\kappa \sin \alpha} \right|^2 \\ &\times \left(\left(1 - \frac{\omega_*}{\omega_r} \right) \frac{\delta f_0}{\delta E} - \frac{\lambda}{E} \frac{\delta f_0}{\delta \lambda} \right), \end{aligned} \quad (44)$$

where v_r is defined by Eq. (38).

(iii) Nonlocal theory: $\Delta_m^{(o)} \leq \Delta_b^t < r_m$

Taking into account the fact that the function G_m is mainly determined by the outer mode structure and using Eqs. (31), (36) and (37), we find from Eq. (11) for $s = 1$ resonance

$$\frac{\gamma}{\omega_r} = \frac{32\sqrt{2\epsilon} q M v_A v_r^6}{B_0^2 R_0 D_1} J_0^2(\xi) \left(\frac{m v_\perp}{r_m, \omega_c} \right) \int_0^{\kappa_{max}^2} \kappa^2 d\kappa^2 \frac{\Delta_m^{(i)}}{r_b^t} \frac{H(W^t)}{W^t} \left(\left(1 - \frac{\omega_*}{\omega_r} \right) \frac{\delta f_0}{\delta E} - \frac{\lambda}{E} \frac{\delta f_0}{\delta \lambda} \right), \quad (45)$$

where $W^t = \Delta_b^t / 2 \Delta_m^{(o)}$, v_r is given by Eq. (38), and all quantities are calculated at $r = r_m$. The function $H(W^t)$ is defined as

$$\begin{aligned} H(W^t) &= \frac{1}{4} \int_{-W^t}^{W^t} dy \left| \int_{-\pi/2}^{\pi/2} d\theta \left[K_0(|y + W^t \cos \alpha|) e^{-i(\alpha+\pi/2)} \right. \right. \\ &+ \left. \left. K_0(|y - W^t \cos \alpha|) e^{-i(\alpha+\pi/2)} \right] \sin \alpha e^{i\kappa \sin \alpha} \right|^2. \end{aligned} \quad (46)$$

The above integrals can be evaluated analytically by approximating $K_0 \approx \pi \delta(y)$ to obtain $H(W^t) = 2\pi^2/W^t$ for $W^t \gg 1$ and $H(W^t) = 2\pi^2 W^t/3$ for $W^t \ll 1$.

The above set of expressions for the linear growth rate of TAEs, Eqs. (26), (32), (34), (40), (44) and (45), modify some pre-factors of Ref. [24]. Moreover, Eq. (32) has been kept in a less simplified form. However, the drive mechanism in the expressions is the same, and the remaining integrands have been rewritten in order to obtain a condition for positive growth rate of bi-directional tornado modes, which is considered next.

C. VELOCITY ANISOTROPY DRIVE FOR TORNADO MODES

We model the ICRH-accelerated protons with a velocity distribution function [23]

$$f_0 = \alpha \bar{\beta} \exp(-E/T) \exp(-(\lambda - \langle \lambda \rangle)^2 / \sigma_\lambda^2) \quad (47)$$

strongly peaked in the pitch angle variable around λ . Here, $\bar{\beta}$ is the peaking parameter indicating the degree of anisotropy, T is the tail temperature and α is a normalisation constant chosen in such a way that

$$\bar{\beta} = \frac{8\pi f_0}{B_0^2} \int_{-\pi}^{\pi} \frac{d\theta}{2\pi} \int d^3p E f_0. \quad (48)$$

In order to analytically estimate the drive of bi-directional tornado modes, we start by rewriting Eq. (20) in order to obtain the velocity anisotropy criterion for driving tornado modes with negative toroidal mode numbers,

$$\sigma_\lambda^2 < \sigma_{\lambda,d}^2 = \left| \frac{T\lambda(\lambda - \lambda\langle\lambda\rangle)}{E \left(1 - \frac{\omega_*}{\omega_r}\right)} \right|. \quad (49)$$

The form of the hot ion velocity distribution function in Eq. (47) is suggested by SELFO modelling [27]. Figure 12 illustrates modelled pitch-angle distribution functions of fast protons for JET Pulse No: 66203. The modelling shows that for energies $E \sim 1\text{MeV}$, the tail temperature is $T = 527\text{keV}$, the pitch-angle centre is $\langle \lambda \rangle = 0.96$, $d\bar{\beta}/dr = -0.12$ and $\bar{\beta} = 0.05$. From Eq. (49), we then find $\sigma_{\lambda,d} = [0.0509, 0.0551, 0.0594]$ for $n = [-6, -5, -4]$, where Eqs. (2) and (3) have been used in order to obtain the values of the safety factor on the three different magnetic flux surfaces and the resonant frequencies, $\omega_r = \omega_{TAE}$, respectively.

We note that the change in σ_λ very well explains the experimental observation in Fig.5 that counter-propagating tornado modes are delayed as compared to co-propagating tornado modes, even though they are associated with the same magnetic flux surface and, hence, the eigenmode solutions appear simultaneously. However, the damping effect due to $d\bar{\beta}/dr$ is too high for counter-propagating tornadoes to be excited together with their corresponding co-propagating tornadoes. As the value of $\sigma_\lambda^{(0)} \in [0.013, 0.065]$ drops below the critical value $\sigma_{\lambda,d}$, determined by Eq. (49), the velocity anisotropy drive for counter-propagating tornadoes becomes larger than the universal damping coming from a monotonic hot ion pressure profile. Since the limit for $n = -6$ is the most restrictive, it does not appear ahead of the $n = -5$ and $n = -4$ tornadoes, which would be the case otherwise.

For the parameters of JET Pulse No: 66203 at 20.2s, we also find that the trapped particle width satisfies $\Delta_b \gg \Delta_m$. Hence, we are in the limit where the narrow banana width approximation is marginally satisfied. Results from CASTOR-K modelling show that this is indeed the case.

CONCLUDING REMARKS AND DISCUSSION

Recent observations on JET have shown that bi-directional tornado modes can be excited by fast ions generated due to ICRH. In the present work the spectrum of bi-directional tornado modes is analysed with a suite of MHD codes in order to determine the radial location, the toroidal mode numbers and the temporal evolution of the modes. Furthermore, the drive mechanism for bidirectional tornado modes both due to passing and trapped fast ions is investigated analytically and a condition for a positive instability growth rate, in terms of the parameters of the fast ion velocity distribution function, is derived and analysed. It is found that the free energy coming from anisotropy of the fast ion velocity distribution function can strongly contribute to the mode excitation. For relevant plasma parameters, it is shown that the excitation condition is satisfied just before a giant sawtooth crash occurs. The results also explain why the counter-propagating tornado modes are excited simultaneously, whereas co-propagating tornado modes are excited one-by-one. The reason is that, due to fast ion velocity space anisotropy, the TAE growth rate becomes positive in the case $n < 0$ for almost identical values of the peaking parameter that characterises the degree of anisotropy.

Modelling by the CASTOR-K code indicates that the small banana width limit in the case of excitation by trapped fast ions is a good approximation for $n = +6$ tornado modes, and a reasonable approximation for $n = +5$ tornado modes. However, it is found that the excitation of $n = +4$ tornado modes is governed by potato-type orbits of the trapped fast ions. Since in our case $r_n = +6 > r_n = +5 > r_n = +4$, this thus indicates that the tornado modes located radially further out have a smaller overlap with potato orbits and, instead, have a larger overlap with banana orbits of trapped fast ions. In the near future, it is our intention to formulate a theory describing excitation of the TAEs by trapped fast ions having potato orbits. We also note that the analytical expressions for the TAE growth rate have been derived by applying a perturbative approach and the results should be verified by using numerical codes. Since at present the CASTOR-K code can only be used for a growth rate calculation for the copropagating TAEs, an extension to the case of bi-directional TAEs would be required. Finally, we emphasize that in order to obtain realistic excitation conditions, the rates due to relevant damping mechanisms should be included in the analysis, which has been omitted in the present paper.

ACKNOWLEDGMENTS

We wish to thank our colleagues who operated the JET tokamak during the experiments modelled here. We also thank Dr. F. Nabais for assessing the applicability of the small banana width approximation with the CASTOR-K code. This work has been conducted under association contracts between EURATOM, Sweden and UK, and was partly funded by the Swedish Research Council.

REFERENCES

- [1]. ITER Physics Basis 1999, Nuclear Fusion **39**, 2137 (1999).
- [2]. S.E. Sharapov, B. Alper, F. Andersson et al., Nuclear Fusion **45**, 1168 (2005).
- [3]. D. Borba, B. Alper, R. V. Budny et al., Nuclear Fusion **40**, 775 (2000).

- [4]. S. von Goeler, W. Stodiek, and N. Sauthoff, *Physical Review Letters* **33**, 1201 (1974).
- [5]. B.B. Kadomtsev, *Soviet Journal of Plasma Physics* **1**, 389 (1976).
- [6]. D. Campbell, D. F. H. Start, J. A. Wesson et al., *Physical Review Letters* **60**, 2148 (1988).
- [7]. F. Porcelli, *Plasma Physics and Controlled Fusion* **33**, 1601 (1991).
- [8]. F. Porcelli, *Physical Review Letters* **66**, 425 (1991).
- [9]. M. Saigusa, H. Kimura, Y. Kusama et al., *Plasma Physics and Controlled Fusion* **40**, 1647 (1998).
- [10]. S. Bernabei, M. G. Bell, R. V. Budny et al., *Physical Review Letters* **84**, 1212 (2000).
- [11]. W.W. Heidbrink, E. D. Fredrickson, T. K. Mau et al., *Nuclear Fusion* **39**, 1369 (1999).
- [12]. G. Y. Fu, *Physics of Plasmas* **2**, 1029 (1995). 20
- [13]. H.L. Berk, J. W. Van Dam, D. Borba, J. Candy, G. T. A. Huysmans, and S. Sharapov, *Physics of Plasmas* **2**, 3401 (1995).
- [14]. G.J. Kramer, S. E. Sharapov, R. Nazikian, N.N. Gorelenkov, and R.V. Budny, *Physical Review Letters* **92**, 015001 (2004).
- [15]. S.E. Sharapov, B. Alper, J. Fessey et al., *Physical Review Letters* **93**, 165001 (2004).
- [16]. B. Alper, S. Hacquin, and S. Sharapov, in *Proc. of the 47th APS Division of Plasma Physics Conference, Denver (American Physical Society, 2005)*, pp. L03.00001.
- [17]. S.E. Sharapov, in *Proc. of the 21st International Conference on Fusion Energy 2006, Chengdu (IAEA, Vienna, 2006)*, pp. EX/P6-19.
- [18]. S. Hacquin, B. Alper, S. Sharapov et al., *Nuclear Fusion* **46**, S714 (2006).
- [19]. G. J. Kramer, C.Z. Cheng, Y. Kusama, R. Nazikian, S. Takeji, and K. Tobita, *Nuclear Fusion* **41**, 1135 (2001).
- [20]. C.Z. Cheng, L. Chen, and M.S. Chance, *Annals of Physics* **161**, 21 (1985).
- [21]. G.Y. Fu and J. W. Van Dam, *Physics of Fluids B* **1**, 1949 (1989).
- [22]. B.N. Breizman and S.E. Sharapov, *Plasma Physics and Controlled Fusion* **37**, 1057 (1995).
- [23]. H.V. Wong and H. L. Berk, *Physics Letters A* **251**, 126 (1999).
- [24]. T.Fülöp, M. Lisak, Ya. I. Kolesnichenko, and D. Anderson, *Plasma Physics and Controlled Fusion* **38**, 811 (1996).
- [25]. B.N. Breizman, H.L. Berk, M.S. Pekker, S.D. Pinches, and S.E. Sharapov, *Physics of Plasmas* **10**, 3649 (2003).
- [26]. M.N. Rosenbluth and H. P. Rutherford, *Physical Review Letters* **34**, 1428 (1975).
- [27]. J.Hedin, T. Hellsten, L.-G. Eriksson, and T. Johnson, *Nuclear Fusion* **42**, 527 (2002).
- [28]. G.T.A. Huysmans, J. P. Goedbloed, and W. Kerner, *Proc. of the CP90 Conference on Computational Physics, Amsterdam (World Scientific, Singapore, 1991)*, p. 371.
- [29]. S. Poedts and E. Schwartz, *Journal of Computational Physics* **105**, 165 (1993).
- [30]. A.B. Mikhailovskii, G.T. A. Huysmans, W.O.K. Kerner, and S.E. Sharapov, *Plasma Physics Reports* **23**, 844 (1997).
- [31]. S.E. Sharapov, A.B. Mikhailovskii, and G.T.A. Huysmans, *Physics of Plasmas* **11**, 2286 (2004).

- [32]. N.P. Young, S.E. Sharapov, and V. M. Nakariakov, *Plasma Physics and Controlled Fusion* **48**, 295 (2006).
- [33]. J. Candy, B. N. Breizman, J.W. Van Dam, and T. Ozeki, *Physics Letters A* **215**, 299 (1996).
- [34]. H.V. Wong, H.L. Berk, and B.N. Breizman, *Nuclear Fusion* **35**, 1721 (1995).
- [35]. H.L. Berk, B.N. Breizman, and H. Ye, *Physics Letters A* **162**, 475 (1992).
- [36]. D. Borba and W. Kerner, *Journal of Computational Physics* **153**, 101 (1999).

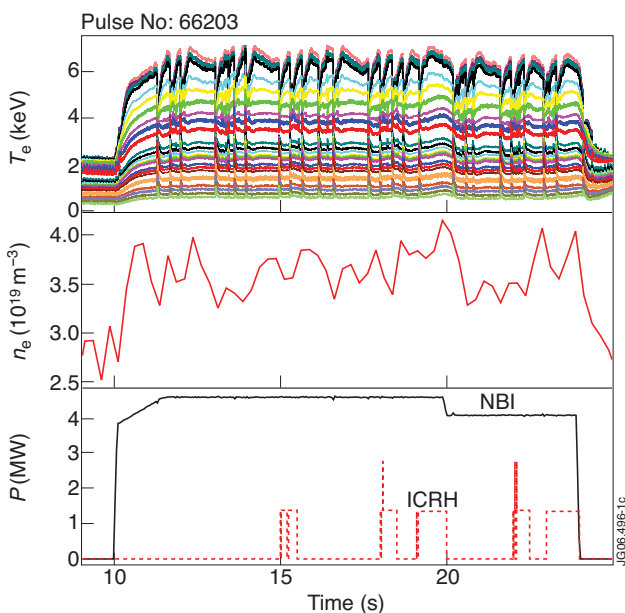


Figure 1: Top: Electron temperature T_e measured with multi-channel ECE diagnostics at different radii on JET. Middle: Electron density $n_e(0)$ measured with LIDAR. Bottom: ICRH (black) and diagnostic NBI (red) power waveforms.

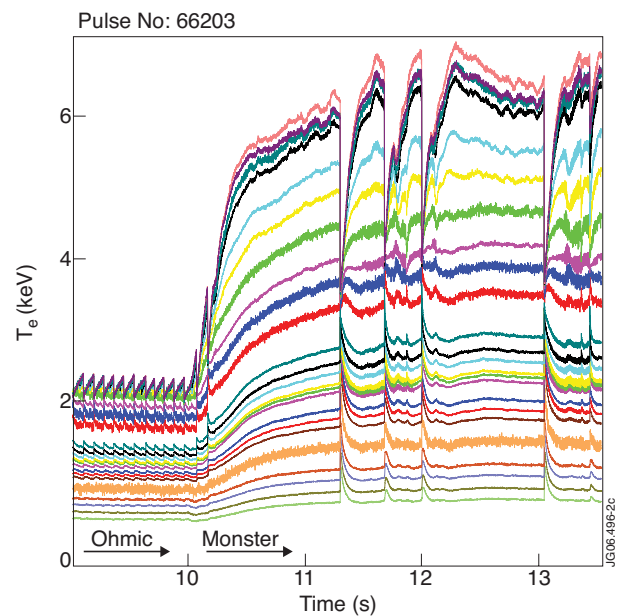


Figure 2: Transition from short-period, ~ 100 ms, Ohmic sawteeth to long-period, ~ 1 s, monster sawteeth, is observed after high power ICRH is applied.

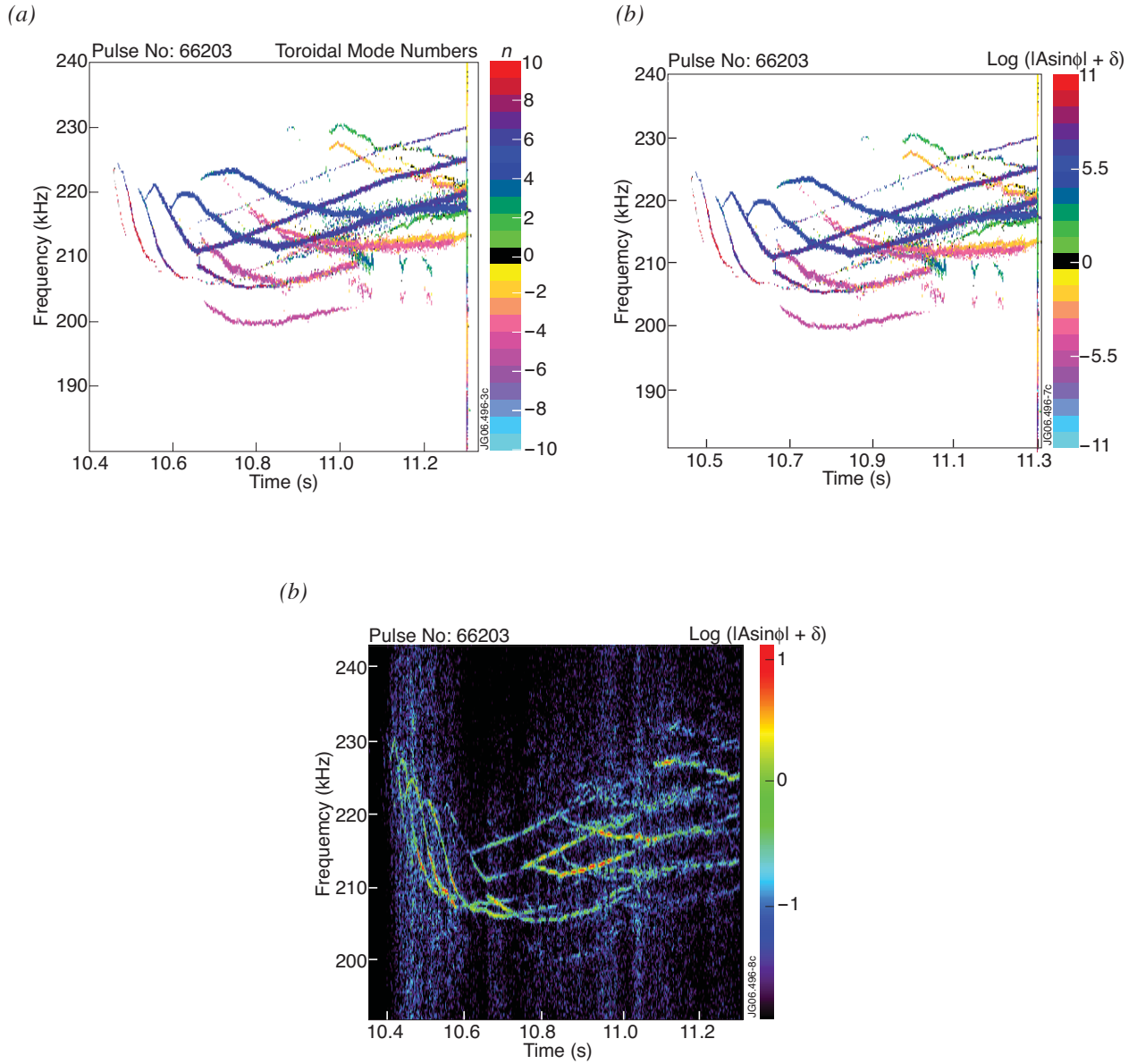


Figure 3: (a) Magnetic spectrogram showing toroidal mode numbers of the observed bidirectional tornado modes preceding the monster sawtooth crash at 11.3s. (b) Zoom of Figure 3 (c) showing tornado modes with both positive and negative mode numbers in the interferometry data (to be compared to Figure 3 (a)). (c) Spectrogram of high-frequency density perturbations measured with the O-mode interferometry (frequency 50.47GHz) [15]. Tornado modes are seen in the TAE frequency range around 200–240kHz, frequency-sweeping Alfvén cascades are seen in the frequency range 50–150kHz.

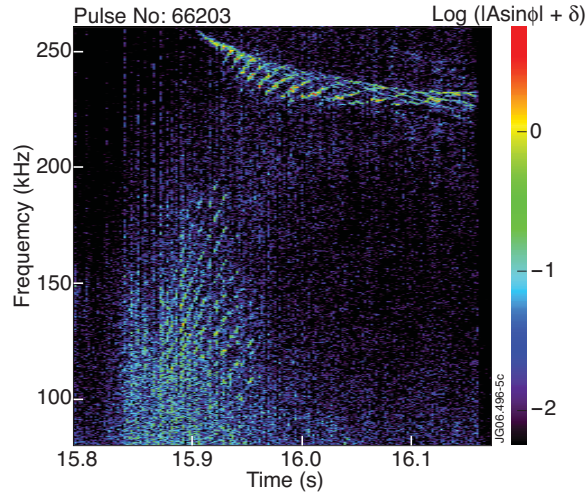


Figure 4: Spectrogram of high-frequency density perturbations measured with the O-mode interferometry (frequency 50.47GHz). Tornado modes are seen in the TAE frequency range around 200–240kHz, frequency-sweeping Alfvén cascades are seen in the frequency range 100–200kHz.

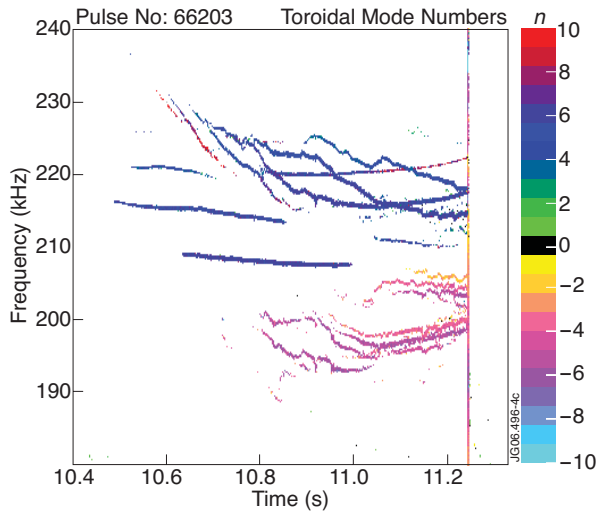


Figure 5: Magnetic spectrogram showing the temporal evolution of tornado modes and TAEs (no chirping) at the time $t = 20.2s$ in JET Pulse No: 66203. From toroidal mode number analysis, tornado modes with both negative and positive mode numbers are identified. Their existence is verified by modelling (Sec. III) and is further motivated by a velocity anisotropy drive estimate (Sec. IV).

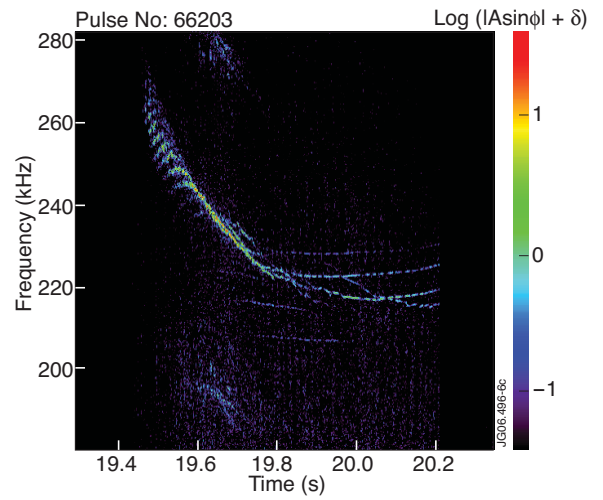


Figure 6: Spectrogram of high-frequency density perturbations measured with the O-mode interferometry (frequency 50.47GHz). Positive tornado modes are seen in the TAE frequency range around 200–240kHz. However, the negative tornado modes, measured by Mirnov coils in Figure 5, are not detected by interferometry.

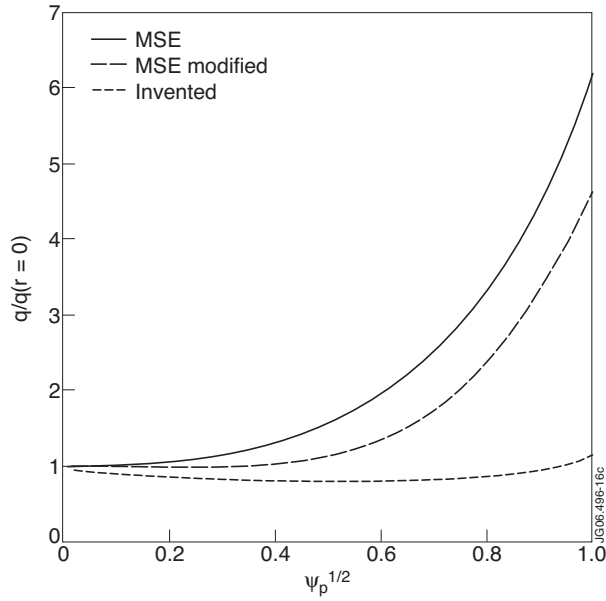


Figure 7: Radial safety factor profiles $q(r)$ normalised to the value on the magnetic axis, $q_0 = q(r = 0)$, as functions of normalised poloidal flux, $\psi_p^{1/2} \sim r/a$, where a is the minor radius of the plasma edge. The three equilibria are the MSE measured equilibrium (solid line), a nonmonotonic modified MSE equilibrium (dashed line) and an invented equilibrium from JET Pulse No: 54956 (dash-dotted line). Variations of the two non-monotonic q -profiles are also modelled.

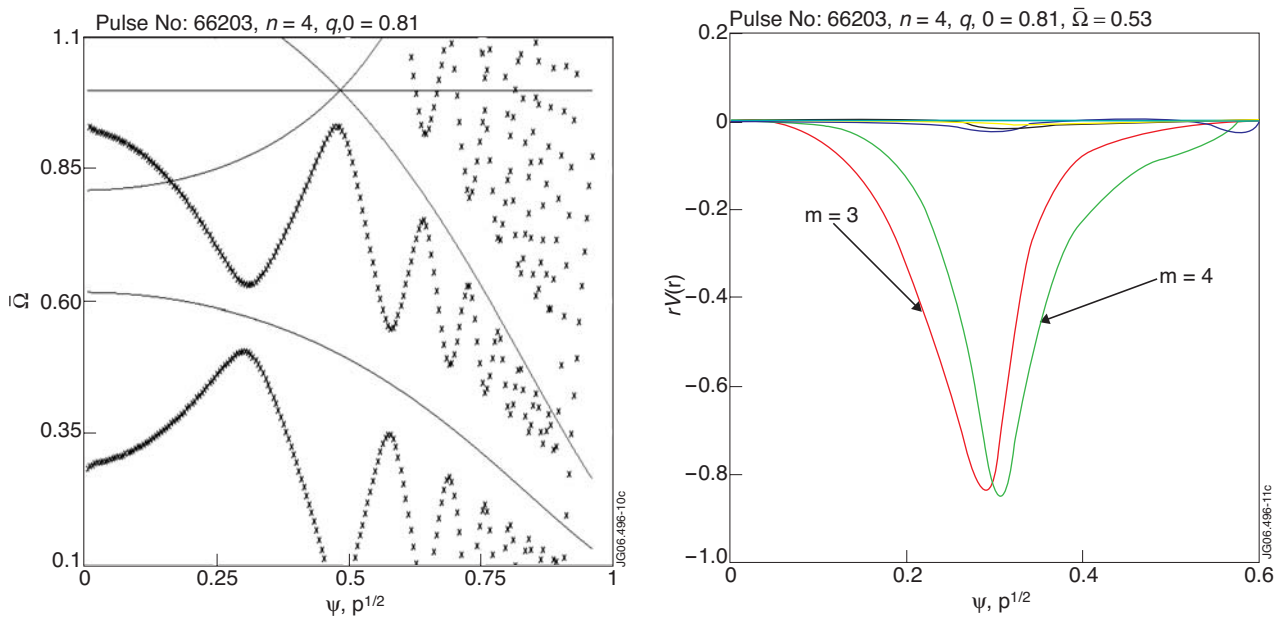


Figure 8: Left: Alfvén continuum gap structure (from CSCAS) for $n = +4$ shear Alfvén waves with a safety factor on magnetic axis $q_0 = 0.81$. Thin lines denote $q(\psi_p^{1/2})$ and $n_e(\psi_p^{1/2}) = \text{const}$ profiles and the central frequencies of TAE and EAE gaps. Right: Mode structure (from MISHKA) of the mode associated with the gap at $\psi_p^{1/2} = 0.31$.

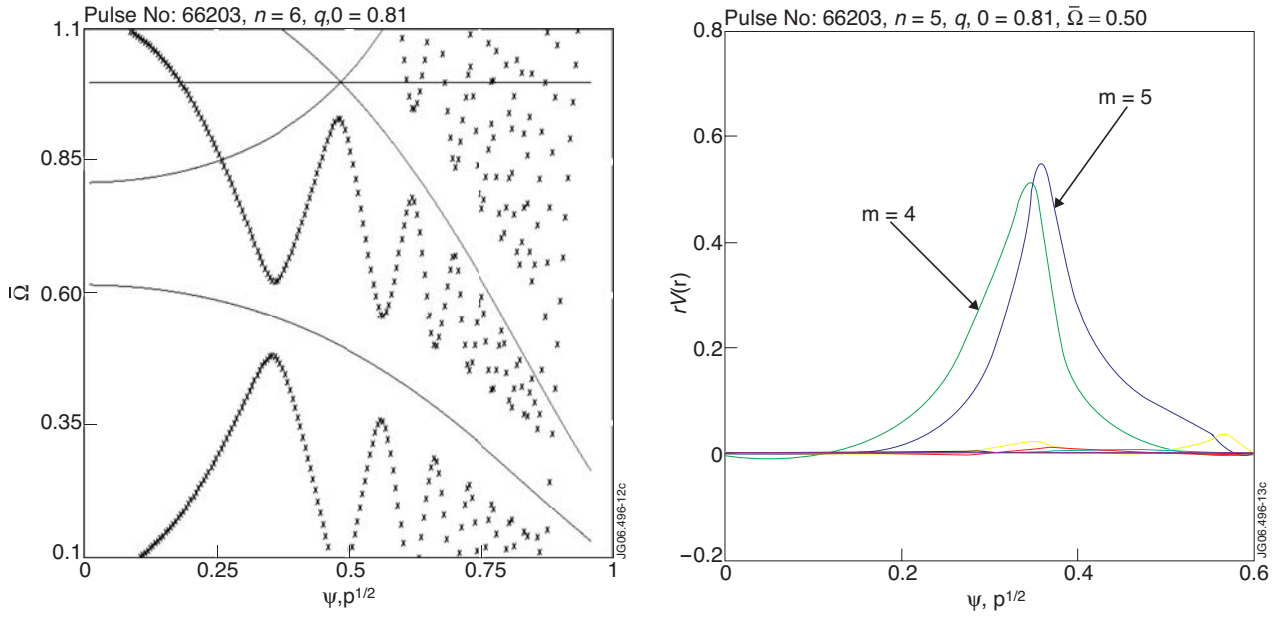


Figure 9: Left: Alfvén continuum gap structure (from CSCAS) for $n = +5$ shear Alfvén waves with a safety factor on magnetic axis $q_0 = 0.81$. Thin lines denote $q(\psi_p^{1/2})$ and $n_e(\psi_p^{1/2}) = \text{const}$ profiles and the central frequencies of TAE and EAE gaps. Right: Mode structure (from MISHKA) of the mode associated with the gap at $\psi_p^{1/2} = 0.36$.

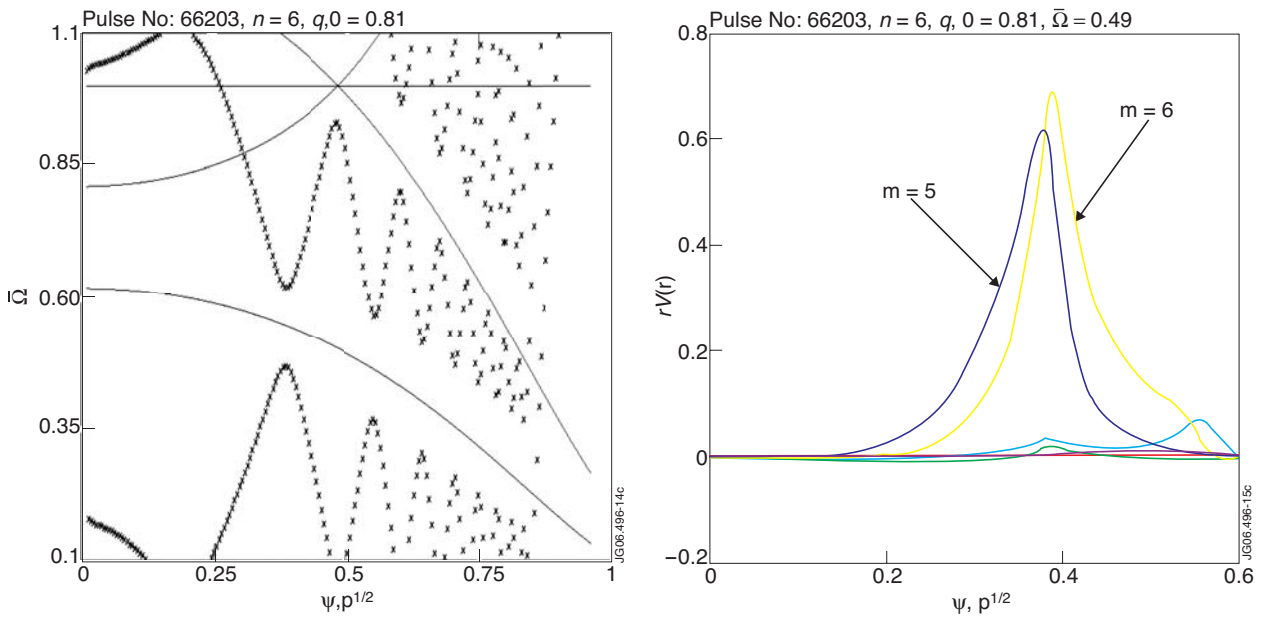


Figure 10: Left: Alfvén continuum gap structure (from CSCAS) for $n = +6$ shear Alfvén waves with a safety factor on magnetic axis $q_0 = 0.81$. Thin lines denote $q(\psi_p^{1/2})$ and $n_e(\psi_p^{1/2}) = \text{const}$ profiles and the central frequencies of TAE and EAE gaps. Right: Mode structure (from MISHKA) of the mode associated with the gap at $\psi_p^{1/2} = 0.39$.

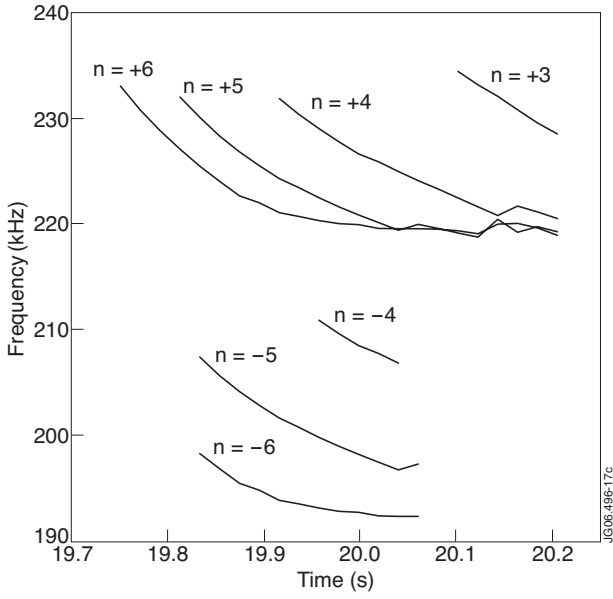


Figure 11: Spectrogram showing the temporal evolution of modelled tornado modes before the sawtooth crash event at $t_{crash} = 20.2s$ in JET Pulse No: 66203. The agreement with experimental data is verified by a comparison with Fig.5. However, the experimental observation of two groups of multiple counter-propagating tornado modes for $t \geq 20.1s$ is not reproduced, as discussed in the text.

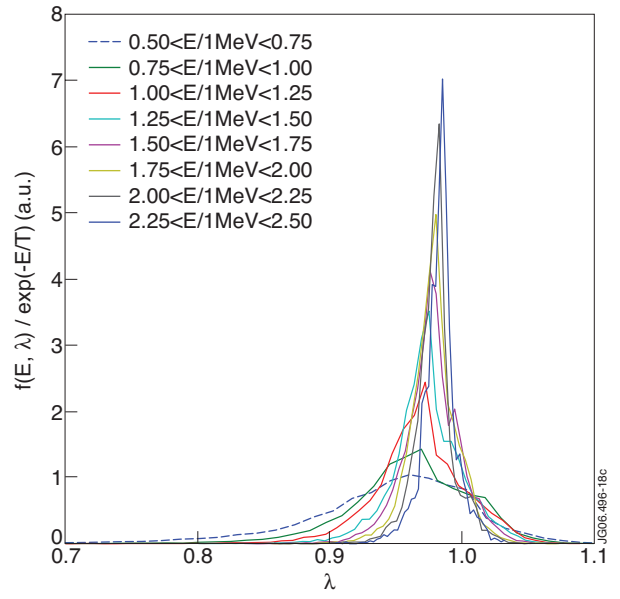


Figure 12: SELFO modelling output showing the hot ion velocity distribution function at different energies. The form of the hot ion velocity distribution function suggests an analytic model given by Eq. (47).